Spectral energetic properties of the X-ray-boosted photoionization by an intense few-cycle laser*

Ge Yu-Cheng(葛愉成)† and He Hai-Ping(何海萍)

School of Physics and State Key Laboratory of Nuclear Physics and Technology, Peking University, Beijing 100871, *China*

(Received 22 October 2013; revised manuscript received 22 December 2013; published online 28 May 2014)

We report a discovery that an intense few-cycle laser pulse passing through gas leaves a fingerprint of its field envelope on the photoelectron energy spectrum, which involves continuous X-ray radiations. The spectrum resulting from the photoionization processes includes significant quantum enhancement and interference and exhibits interesting energetic properties. The spectral cut-off energies reflect the strength, time, and interference of the laser field modulation on the photoelectron energy. These energetic properties suggest a new method for precise intense-laser-pulse measurement *in situ*. The method has the advantages of accuracy, simplicity, speed, and large dynamic ranges (up to many orders of intensity).

Keywords: laser intensity, pulse duration, X-ray-boosted photoionization, energetic properties of photoelectron energy spectrum

PACS: 42.65.Re, 42.50.Hz, 42.50.Ct, 42.60.Jf **DOI:** 10.1088/1674-1056/23/7/074207

1. Introduction

With the development of laser technology, producing pulses with ultrashort durations or ultra-high field strengths has attracted increasing interest. Lasers with pulse durations that rival a single optical cycle (e.g., 2.7 fs at 800 nm) or less are commercially available.[1,2] A large facility can produce intensities in excess of 10^{18} W/cm^2 or up to 10^{22} W/cm^2.[3] Ultrashort intense lasers have been used as pump pulses for above-threshold ionizations (ATIs)[4] and high-order harmonic generation,[5–7] and have also been employed in the study of nonlinear Compton scattering[8] and laser acceleration.[9] The absolute laser frequency can be precisely measured by using a femtosecond optical frequency comb,[10–12] but to determine the peak intensity I, field envelope $F(t)$, and carrier-envelope phase Φ of each pulse in real time is challenging. These parameters cannot be measured directly accurately because few detectors would survive such intense fields without being damaged. However, knowledge of these optical parameters is critical to the production and use of intense laser pulses.

Laser intensities are usually estimated by using four optical parameters: the focal spot size, the pulse energy, the time-independent spatial profile of the beam, and the temporal profile of the laser beam, which can be measured with an autocorrelation method.[13] The spatial intensity can be imaged using a digital camera while the spatial wave-front can be measured by a Shack–Hartmann sensor[14,15] or by shearing interferometry.[16,17] Obviously, the estimation is subject to a variety of errors that rapidly sum to a large uncertainty in the intensity.[18] More recently proposed measurement techniques include measuring the field ionization of highly charged inert gases ($I \approx 10^{20}$ W/cm^2),[19,20] Thomson scattering from single and multiple electrons ($I \geq 10^{18}$ W/cm^2), and the momentum transferred to the photoion and photoelectron.[21,22] Because of the lack of structure in laser-induced ionization spectra, it is difficult to extract both the intensity I and the field envelope $F(t)$ (time t, duration $\tau_{\rm L}$, carrier-envelope phase Φ) of an intense laser pulse.

Calculations of the photoelectron energy spectra (PES) excited by a continuous X ray and an intense laser pulse that have been cross-correlated in time and space show that (i) photoionization is always significantly enhanced by the ATI because of X rays (we call this phenomenon X-ray-boosted photoionization, or XBP) and (ii) the PES includes fine structures and regular fluctuations. In this study, we present the use of XBP spectroscopy for the measurement of an intense laser pulse *in situ*. Our method is based on an analysis of the energetic properties of a measured PES. The method presents the advantages of accuracy, simplicity, speed, and large dynamic range (up to many orders of intensity).

The rest of this paper is organized as follows. Section 2 is divided into five subsections, where we use the strong field approximation (SFA)[23] to calculate the PES at the single-atom level for two correlation modes (0° and 90°) between the X ray and laser. The quantum interference and field modulation caused by the XBP are theoretically analyzed. In Section 3, the quantum-mechanically calculated PES and the classical predictions are compared. Formulas for pulse reconstruction from the XBP's energetic properties are presented. Finally, we summarize the findings in Section 4.

*Project supported by the National Natural Science Foundation of China (Grant No. 11175010).

†Corresponding author. E-mail: gyc@pku.edu.cn

© 2014 Chinese Physical Society and IOP Publishing Ltd

2. X-ray-boosted photoionization

Before introducing the formulas for pulse reconstruction and measurement, we theoretically investigate the XBP spectra generated by a continuous X-ray beam and intense laser pulses with different CEP values.

2.1. Strong field approximation

In cross correlation between an intense laser pulse and a continuous narrow-band X ray (both co-propagating collinearly in the Z direction, called 0° correlation, see Fig. 1(a)), electron motion satisfies the time-dependent Shrödinger equation (in atomic units)

$$i\frac{\partial}{\partial t}\Psi(\boldsymbol{r},t)=\left[-\frac{1}{2}\nabla^2-\frac{1}{r}-\boldsymbol{r}\cdot\boldsymbol{E}(t)\right]\Psi(\boldsymbol{r},t), \tag{1}$$

where $\boldsymbol{r}=(x,y,z)$ denotes the space coordinates, and $\Psi(\boldsymbol{r},t)$ represents the electron wave function. The electric field $\boldsymbol{E}(t)=\boldsymbol{E}_{\rm L}(t)+\boldsymbol{E}_{\rm X}(t)$ comprises the contribution of a linearly polarized laser field, $\boldsymbol{E}_{\rm L}(t)=[E_0F(t)\cos(\omega_{\rm L}t+\Phi),0,0]$, and an X-ray field, $\boldsymbol{E}_{\rm X}(t)=[E_{\rm X}\cos(\omega_{\rm X}t),0,0]$, where E_0 ($\omega_{\rm L}$) and $E_{\rm X}$ ($\omega_{\rm X}$) are laser and X-ray electric field amplitudes (angular frequencies), respectively. The $F(t)$ is the envelope function of the laser electric field. The electric field $\boldsymbol{E}(t)$ is related to the vector potential $\boldsymbol{A}(t)$ by $\boldsymbol{E}(t)=-(1/c)\partial_t\boldsymbol{A}(t)$, where c is the velocity of light in vacuum. Equation (1) can be solved analytically within the SFA.[23] As a result, the Coulomb continuum eigenfunctions may be substituted by plane waves, and equation (1) is integrated by

$$\Psi(\boldsymbol{r},t)=\mathrm{e}^{\mathrm{i}I_{\rm p}t}\left[|0\rangle+\int\mathrm{d}^3\boldsymbol{p}b(\boldsymbol{p},t)|\boldsymbol{p}\rangle\right]. \tag{2}$$

Here $|0\rangle$ denotes the atomic ground state with ionization potential of $I_{\rm p}$. The plane wave is given by $|\boldsymbol{p}\rangle=\exp(\mathrm{i}\boldsymbol{p}\cdot\boldsymbol{r})$, with $\boldsymbol{p}$ being the electron momentum, and $b(\boldsymbol{p},t)$ the momentum space wave function of free electrons. Within the SFA, the probability amplitude for the transition from $|0\rangle$ to a final state $|\boldsymbol{p}\rangle$ is given by

$$b(\boldsymbol{p})=\mathrm{i}\int_{-\infty}^{\infty}\mathrm{d}t\boldsymbol{E}(t)\cdot\boldsymbol{d}[\boldsymbol{p}-\boldsymbol{A}(t)]\,\mathrm{e}^{-\mathrm{i}\widetilde{S}(t)}, \tag{3}$$

where $\widetilde{S}(t)$ is the quasi-classical action,

$$\widetilde{S}(t)=\int_t^{\infty}\mathrm{d}t'[\boldsymbol{p}-\boldsymbol{A}(t')]^2/2+I_{\rm p}t, \tag{4}$$

$\boldsymbol{d}(\boldsymbol{p})=\langle\boldsymbol{p}|\boldsymbol{x}|0\rangle$ denotes the atomic dipole matrix element for the bound–free transition, and $d_x(\boldsymbol{p})$ is the component parallel to the polarization axis. The above discussion also applies to the 90°-correlation measurement where the X ray propagates in the Y direction (Fig. 1(b)). In the remainder of this paper, atomic units and hydrogen atoms are used for simplicity ($I_{\rm p}=13.6$ eV, $d_x(\boldsymbol{p})=\mathrm{i}2^{19/4}I_{\rm p}^{5/4}\boldsymbol{p}/\pi(2I_{\rm p}+\boldsymbol{p}^2)^3$ for s state). Obviously, $b(\boldsymbol{p})$ describes the quantum interference between electron wave packets generated at different times, and each detected electron carries the pulse and atomic information corresponding to the entire interaction time domain.

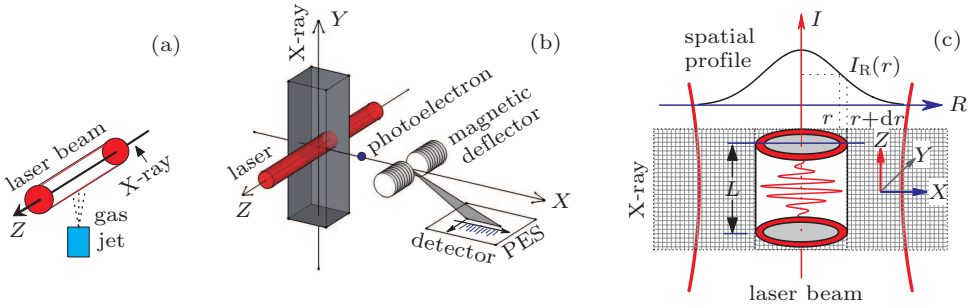


Fig. 1. (color online) Illustrations of the XBP setup. (a) 0° correlation between an X ray and a laser pulse. (b) 90° correlation between an X ray and a laser pulse. The X ray may be filtered from the Thomson scattering radiation,[8] or the high-order radiation generated by a synchronized picosecond intense laser (usually split from a primary beam before pulse compression).[24–26] Photoelectrons that leave the interaction region are deflected by a magnetic field and collected by a spectrometer. The photoelectrons with the specific energies of interest are selected by adjusting the magnetic field. (c) A spatial profile of the laser intensity, $I_{\rm R}(r)=\exp[-4\ln 2(r)^2/\tau_{\rm R}^2]$ (black curve), and an iso-intensity shell in the interaction volume (radius r, thickness $\mathrm{d}r$, and length L).

Physically, $|b(\boldsymbol{p})|^2$ is the photoelectron momentum spectrum $n(\boldsymbol{p})$, and its conversion to the PES is given by $n(W)=|b(\boldsymbol{p})|^2/\sqrt{2W}$, where W is the photoelectron energy, and $b(\boldsymbol{p})$ can be expressed as $b(\boldsymbol{p})=b_1(\boldsymbol{p})+\varepsilon$, where

$$\begin{aligned}b_1(\boldsymbol{p}) &= \frac{1}{2}\mathrm{i}\int_{-\infty}^{\infty}\mathrm{d}tE_{\rm X}d_x[\boldsymbol{p}-\boldsymbol{A}(t)]\,\mathrm{e}^{-\mathrm{i}\widetilde{S}_1(t)}\\ &= \frac{1}{2}\mathrm{i}E_{\rm X}\int_{-\infty}^{\infty}\mathrm{d}td_x[\boldsymbol{p}-\boldsymbol{A}(t)]\,\mathrm{e}^{-\mathrm{i}\widetilde{S}_1(t)}\end{aligned} \tag{5}$$

is the dominant term contributed by the X-ray flux and ε is the residual term, which includes the laser contribution. The quasi-classical action of $b_1(\boldsymbol{p})$ is

$$\widetilde{S}_1(t)=\int_t^{\infty}\mathrm{d}t'[\boldsymbol{p}-\boldsymbol{A}(t')]^2/2+(\omega_{\rm X}-I_{\rm p})t. \tag{6}$$

In the following calculations, the laser envelope

$$F(t)=\exp\left[-4\ln 2\frac{t^2}{\tau_{\rm L}^2}\right] \tag{7}$$

is a Gaussian-like time function with a full width at half maxi-

mum (FWHM) of τ_L. The laser peak intensity is calculated as $I = E_0^2/2$, and the electron ponderomotive energy is calculated as $U_p = I/2\omega_L^2$. In discussing the total volumetric XBP production, we must consider the spatial distribution of the laser intensity. For example, figure 1(c) presents a Gaussian-like spatial profile,

$$I_R(r) = \exp\left[-4\ln 2\frac{r^2}{\tau_R^2}\right], \tag{8}$$

where τ_R is the FWHM of the laser beam.

2.2. Single-intensity (SI) and volume-integral (VI) measurements

According to Eq. (3), laser pulses with different intensities can produce photoelectrons with the same momentum $\boldsymbol{p}$ with different probability amplitudes. Usually, it is impossible to produce laser pulses with an absolute single intensity because of parameter fluctuations and jitters in time and space. Therefore, the photoelectrons with energy W are generated by laser pulses with different intensities. Considering the entire distribution, the laser can be considered to have a single intensity I, as long as (i) the pulse intensities are stabilized and controlled within a small range and (ii) the X ray is spatially located in a region in which the laser intensity is constant (or at least approximately constant). The PES is classified into two kinds: single-intensity (SI) or volume-integral (VI), depending on whether it is calculated (measured) by excluding or including, respectively, the contributions from laser intensities ($< I$). The SI PES data can be obtained by a 0°-correlation measurement in which a smaller X ray is intensity-uniformly dressed by the laser beam, while the VI data can be obtained by either a 0°-correlation measurement (where the X-ray intensity is spatially uniform within the laser beam size) or a 90°-correlation measurement (e.g., taking an X-ray photograph of a laser pulse, Fig. 1(b)).

2.3. PES calculation

The black line in Fig. 2(a) shows the SI data for an XBP PES, $n(W)$, calculated with a laser wavelength of $\lambda_L =$ 750 nm, $\tau_L = 7$ fs, $\Phi = 0°$, $I = 5\times10^{14}$ W/cm^2, $\theta = 0°$, and $\omega_X = 1$ keV. Here, the laser intensities are selected so that the depletion of the ground state can be neglected, ensuring the validity of the SFA calculations.[27] The X-ray intensity I_X is set as 5.411×10^8 W/cm^2 without any specific considerations because $n(W)$ is proportional to $I_X = E_X^2/2$, where the factor E_X^2 is included in the expression for $|b(\boldsymbol{p})|^2$ as a constant. The keV or lower-energy X rays can be filtered from the Thomson scattering radiation,[28] or the high-order radiation generated by a synchronized picosecond intense laser (usually split from a primary beam before pulse compression).[24–26] The X-ray intensities at the level of 10^8 W/cm^2 or much higher are feasible in experiments.[26] The parameter θ is an observation angle between the photoelectron momentum $\boldsymbol{p}$ and the laser polarization. The red line in Fig. 2(a) represents the laser-induced contribution, $n_L(W)$. The spectra clearly show two measurable portions (both with clear borders). (i) $W < W_L = 140.364$ eV, which is primarily derived from the laser field (ATI). However, the physics of the ATI is more complicated at low energies[28,29] and is not within the scope of our investigation. The data shown here are only the results calculated within the SFA at the single-atom level. (ii) $W_{a-} = 568.854$ eV $< W <$ 1525.539 eV $= W_{b+}$, which is fully derived from $b(\boldsymbol{p})$ (XBP PES). The lower (upper) cut-off energy denoted by W_a (W_b) is the position of the peak at the low (high) end of the PES ($W_a = 590.200$ eV, $W_b = 1471.481$ eV). The actual PES cut-off energies, W_{a-} and W_{b+}, are slightly less than W_a and greater than W_b, respectively.

According to Fig. 2(a), $n(W)$ is significantly enhanced by the ATI spectrum, with W ranging from W_{a-} to W_{b+} because of the X ray, where the ATI spectrum $n_L(W)$ can be neglected in comparison to $n(W)$, which indicates that the XBP spectrum $n(W)$ is entirely a physical result of the X-ray photoionization, the laser field modulation, and the quantum interference. The irrelevance of the XBP to the ATI is the basis for establishing the relationships between the laser pulse parameters and the XBP energetic and statistical properties. However, this irrelevance will not hold if the laser intensity increases or/and the X-ray photon energy decreases to a value at which the XBP spectrum cannot be neglected in comparison to the ATI spectrum.

2.4. Laser field modulation and quantum interference in XBP

The effects of laser field modulation and quantum interference on the PES are of great interest. The complicated XBP spectral structures show that the quantum interference between electron wave packets is very strong. The thin solid line in Fig. 2(b) shows two expended areas of the SI $n(W)$ (815 eV $< W <$ 850 eV; 1115 eV $< W <$ 1150 eV). This $n(W)$ consists of local small peaks (fine structures). The heavy red line in Fig. 2(b) plots a spectrum that is adjacently averaged from $n(W)$ with a window of 8 eV. With a state-of-the-art photoelectron energy spectrometer, $n(W)$ can be measured with a high energy resolution, while the adjacently averaged spectrum can be measured with a low energy resolution.

Physically, quantum interference occurs because the photoelectrons generated at different times t acquire different

phase factors $\exp[-\mathrm{i}\widetilde{S}(t)]$ (Eq. (3)) in the laser field. Quantitative analysis indicates that, (i) the field modulation of the photoelectron energy, which determines the overall distribution of the PES $n(W)$, results from the oscillating factor $E_0F(t)\cos(\omega_\mathrm{L}t+\Phi)$ included in $\boldsymbol{E}(t)$ (a linear term of $b(\boldsymbol{p})$, Eq. (3)), where $E_0\propto I^{1/2}$ is the modulation strength, and (ii) the fine structures of $n(W)$ result from the factor $E_0F(t)\sin(\omega_\mathrm{L}t+\Phi)$ (or $\boldsymbol{A}(t)$) included in the quasi-classical action $\widetilde{S}(t)$. The red line in Fig. 2(b) represents the laser field modulation of the photoelectron energy. Because $A_\mathrm{L}(t)$ changes slowly at the phases $\omega_\mathrm{L}t+\Phi$ close to $\pi/2$, the photoelectrons have very similar energies and phase factors, and a wide peak at W_b occurs (e.g., 16.54 eV in FWHM, Figs. 2(a) and 2(c)).

2.5. Pulse fingerprint

The oscillating line in the inset of Fig. 2(a) corresponds to

$$W(t) = W_0+2U_\mathrm{p}F^2(t)\sin^2(\omega_\mathrm{L}t+\Phi) + \sqrt{8U_\mathrm{p}W_0}F(t)\sin(\omega_\mathrm{L}t+\Phi), \tag{9}$$

where $W(t)$ is the classical prediction of the final energy of a photoelectron generated at t and moving at $\theta=0^\circ$. The classical prediction of the photoelectron final momentum is

$$\boldsymbol{p}(t)=\boldsymbol{p}_0+2\sqrt{U_\mathrm{p}}F(t)\sin(\omega_\mathrm{L}t+\Phi), \tag{10}$$

where $\boldsymbol{p}_0=\sqrt{2W_0}$ and $W_0=\omega_\mathrm{X}-I_\mathrm{p}$. Equation (10) is the stationary point equation, which is derived from the stationary point of the quasi-classical action $\widetilde{S}_1(t)$ (Eq. (11), the definition of the stationary point in Section 3.1). The relatively higher peak positions of $n(W)$ (SI data, see the black lines in Figs. 2(a) and 2(c)) correspond to the times at which the laser field reaches different extremes. The peak data represent a fingerprint of the field envelope $F(t)$ left by the laser pulse as it passes through the gas. However, the fingerprint disappears in the VI data of $n(W)$, as shown in Fig. 2(d). Obviously, the SI $n(W)$ (Fig. 2(c)) preserves some energetic properties associated with the pulse information (τ_L, Φ, I), while the VI $n(W)$ (Fig. 2(d)) lacks them, but both the SI $n(W)$ and VI $n(W)$ have useful statistical properties. The pattern of the pulse fingerprint provides a new approach to identifying the pulsing field.

Because the statistical properties of the X-ray-boosted photoionization with an intense laser pulse are very different from the energetic properties, they will be discussed in detail in the future.

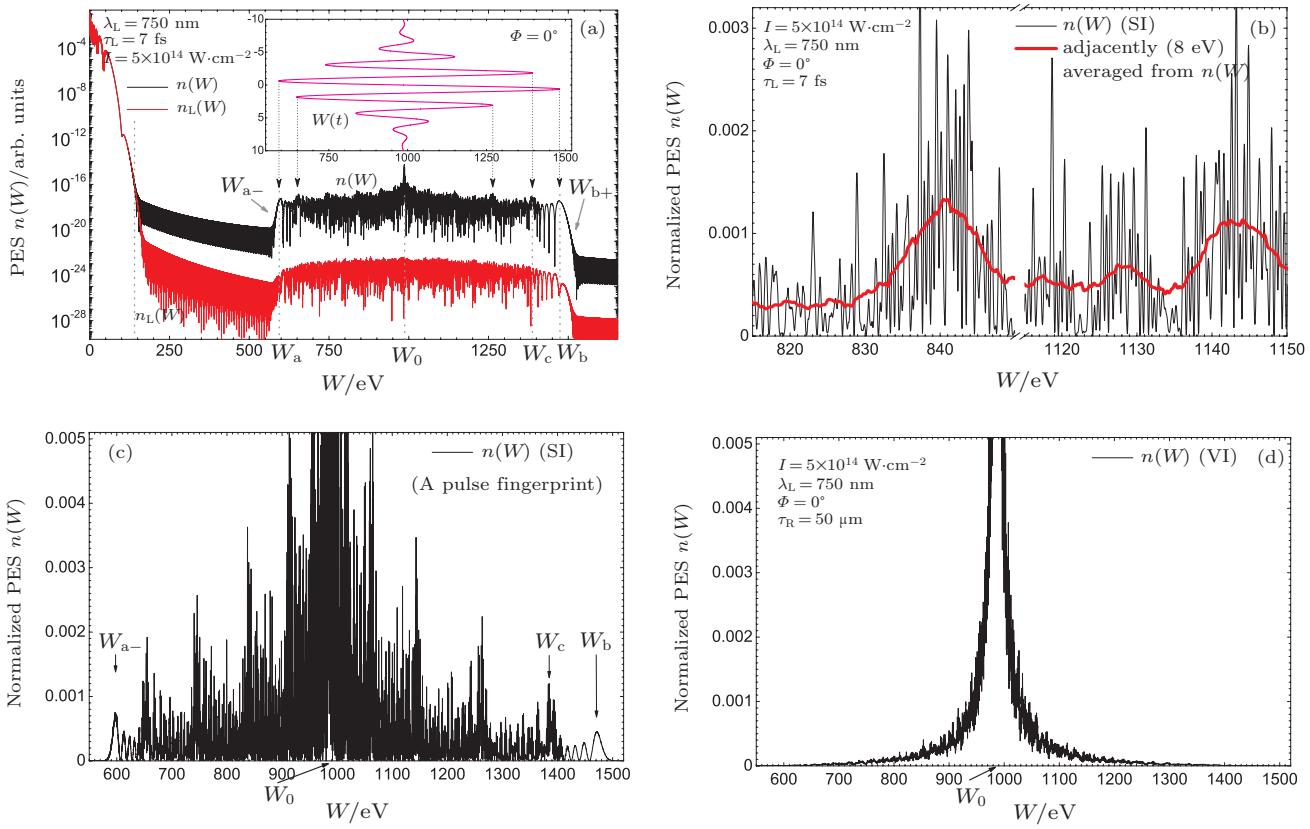


Fig. 2. (color online) XBP photoelectron energy spectra. (a) Black line: SI data based on $n(W)=|b(\boldsymbol{p})|^2/\sqrt{2W}$; red line: the laser-induced contribution $n_\mathrm{L}(W)$. (b) Two expanded areas of $n(W)$ (815 eV $< W <$ 850 eV; 1115 eV $< W <$ 1150 eV). Thin solid line: SI $n(W)$ (normalized); heavy red line: adjacently averaged $n(W)$ using an 8-eV window. (c) SI data based on $n(W)$ (normalized), a fingerprint of the laser pulse. (d) VI $n(W)$ data (normalized) calculated using $\tau_\mathrm{R}=50$ μm.

3. XBP's energetic properties and pulse reconstruction

Because the laser field modulation of the photoelectron energy depends on the factors $E_0F(t)\cos(\omega_L t+\Phi)$ ($E_0 \propto I^{1/2}$), we derive analytical formulas to calculate the parameters τ_L, Φ, and I from the XBP energetic properties for laser pulse reconstruction.

3.1. Classical predictions of the XBP PES

In the time domain, the quasi-classical action $\widetilde{S}_1(t)$ has many stationary points $t_{st,j}$ ($j=1,2,\ldots$) for each momentum $\boldsymbol{p}$, where

$$\frac{\mathrm{d}\widetilde{S}_1(t)}{\mathrm{d}t}\Big|_{t=t_{st,j}} = \frac{[\boldsymbol{p}-\boldsymbol{A}(t_{st,j})]^2}{2}-(\omega_X-I_p) \equiv 0. \tag{11}$$

Equation (11) is the stationary point equation, which determines the initial kinetic energy of the generated photoelectron $W_0=[\boldsymbol{p}-\boldsymbol{A}_L(t_{st,j})]^2/2\equiv\omega_X-I_p$. Equations (9) and (10) are derived from Eq. (11). At time $t=t_{st,j}+\Delta t$ (Δt is small), the transition probability amplitude can be calculated by

$$\Delta b_1(\boldsymbol{p},t_{st,j}) = \frac{1}{2}\mathrm{i}\int_{t_{st,j}}^{t_{st,j}+\Delta t}\mathrm{d}t E_X d_x[\boldsymbol{p}-\boldsymbol{A}(t)]\,\mathrm{e}^{-\mathrm{i}\widetilde{S}_1(t)} = \frac{1}{2}i\Delta t E_X d_x[\boldsymbol{p}-\boldsymbol{A}(t_{st,j})]\,\mathrm{e}^{-\mathrm{i}\widetilde{S}_1(t_{st,j})}. \tag{12}$$

Note that $b_1(\boldsymbol{p},t_{st,j})$ is proportional to Δt. We define an instantaneous time rate of transition probability amplitude $b_1(\boldsymbol{p},t_{st}) \equiv \sum_j \Delta b_1(\boldsymbol{p},t_{st,j})/\Delta t$ as the semi-classical prediction of $b(\boldsymbol{p})$, namely,

$$b_1(\boldsymbol{p}_{st},t_{st}) = \sum_j \frac{1}{2}\mathrm{i}E_X d_x[\boldsymbol{p}-\boldsymbol{A}(t_{st,j})]\,\mathrm{e}^{-\mathrm{i}\widetilde{S}_1(t_{st,j})}. \tag{13}$$

The semi-classical prediction of the PES is $n_{sc}(W) \equiv |b_1(\boldsymbol{p},t_{st})|^2/\sqrt{2W}$. The dotted line in Fig. 3 represents $n_{sc}(W)$ of an SI PES $n(W)$ (the black line in Fig. 2(c)).

3.2. Formulas for pulse reconstruction

To compare the semiclassical prediction $n_{sc}(W)$ with the PES $n(W)$, $n(W)$ is divided by the square of the pulse area ΔT

$$\Delta T \equiv \int_{-\infty}^{+\infty} F^2(t)\,\mathrm{d}t, \tag{14}$$

and

$$n_q(W) \equiv \frac{n(W)}{\Delta T^2} = \frac{|b(\boldsymbol{p})/\Delta T|^2}{\sqrt{2W}}. \tag{15}$$

Because the time dependence of the laser electric field is $E_L(t)=E_0F(t)\cos(\omega_L t+\Phi)$, the laser intensity profile is $E_0^2F^2(t)/2$, where the time function $F^2(t)$ has a dimensionless amplitude of 1 and the shape of the laser intensity is $F^2(t)$. The ΔT (Eq. (14)) represents the time average of the pulse. The reason to divide $n(W)$ by ΔT^2 (Eq. (15)) is that the semiclassical prediction $n_{sc}(W)=|b_1(\boldsymbol{p},t_{st})|^2/\sqrt{2W}$ and the PES $n(W)=|b(\boldsymbol{p})|^2/\sqrt{2W}$ have different dimensionalities, i.e., $b_1(\boldsymbol{p},t_{st})$ is an instantaneous time rate of transition probability amplitude according to its definition (Eqs. (12) and (13)), but $b(\boldsymbol{p})$ is a time integral (Eq. (3)).

The laser pulse information (τ_L, Φ, I) can be retrieved directly from the SI fingerprint data. The solid line in Fig. 3 shows the values of $n_{qs}(W)$ that were adjacently averaged from $n_q(W)$ (Eq. (15)) using a window of 8 eV. We see that (i) the semi-classical predictions (the dotted line in Fig. 3) represent the average values of $n_q(W)$, (ii) the peak positions of $n_{sc}(W)$ (W_1, W_2, W_3) are close to those of $n_{qs}(W)$ (W_a, W_b, W_c), and (iii) $n_{sc}(W)$ only approximates $n_{qs}(W)$ at Φ near 0 or π; otherwise, the pattern of $n_{qs}(W)$ clearly deviates from $n_{sc}(W)$ because of strong interference. However, the fingerprint data, which are measured with a locked CEP of 0 or π, are very useful for calibrating the pulse measurement. For example, with $W_1=591.280$ eV, $W_2=1482.120$ eV, and $W_3=1396.200$ eV, assigning the momentum shifts $\Delta p_{1,2,3} \equiv p_{1,2,3}-p_0=\sqrt{2W_{1,2,3}}-\sqrt{2W_0}$ to the stationary equations $\Delta p_{1,2,3}=2\sqrt{U_p}F(t)\sin(\omega_L t+\Phi)$, where phase $\omega_L t+\Phi=-\pi/2,\pi/2,-3\pi/2$, respectively, gives

$$\omega_L^2\tau_L^2 = \frac{8\pi^2\ln(2)}{\ln(\Delta p_2/\Delta p_3)},\quad \Phi=\frac{\pi\ln(-\Delta p_1/\Delta p_2)}{\ln(\Delta p_2/\Delta p_3)},\quad \sqrt{U_p}=\frac{\Delta p_2}{2}\exp\left[\frac{\ln(2)(\pi-2\Phi)^2}{\omega_L^2\tau_L^2}\right], \tag{16}$$

and solutions of (τ_L, Φ, I) = (7.061 fs, $-0.080°$, 5×10^{14} W/cm^2), which are in good agreement with the input data of (7 fs, 0°, 5×10^{14} W/cm^2). Similarly, using the peak positions (W_1, W_2, W_3) that correspond to $\omega_L t+\Phi=-\pi/2,\pi/2,3\pi/2$, respectively, the formulas change into

$$\omega_L^2\tau_L^2 = \frac{8\pi^2\ln(2)}{\ln(\Delta p_1/\Delta p_3)-2\ln(\Delta p_1/\Delta p_2)},\quad \Phi=\frac{\pi\ln(\Delta p_1/\Delta p_2)}{\ln(\Delta p_1/\Delta p_3)-2\ln(\Delta p_1/\Delta p_2)},\quad \sqrt{U_p}=\frac{\Delta p_2}{2}\exp\left[\frac{2\ln(2)(\pi+2\Phi)^2}{\omega_L^2\tau_L^2}\right]. \tag{17}$$

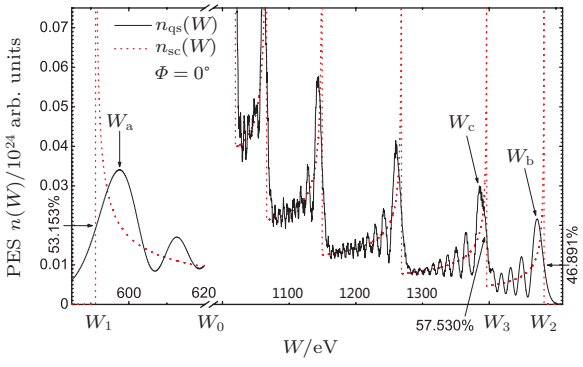


Fig. 3. (color online) XBP energetic properties. Solid line: $n_{qs}(W)$, which is smoothed from $n_q(W)=n(W)/\Delta T^2$. Dotted line: the semi-classical prediction $n_{sc}(W)$. $n(W)$ and $n_{sc}(W)$ are calculated with $\lambda_L=750$ nm, $\tau_L=7$ fs, $I=5\times10^{14}$ W/cm^2, $\omega_X=1$ keV, and $\Phi=0°$.

3.3. Two-step pulse reconstruction

The semi-classical predictions W_1, W_2, and W_3 could not be measured in this experiment, but we can theoretically calculate the following three ratios:

$$\begin{aligned}\varepsilon_1 &\equiv n_{\rm qs}(W_1)/n_{\rm qs}(W_{\rm a}) = n_s(W_1)/n_s(W_{\rm a}),\\ \varepsilon_2 &\equiv n_{\rm qs}(W_2)/n_{\rm qs}(W_{\rm b}) = n_{\rm s}(W_2)/n_{\rm s}(W_{\rm b}),\\ \varepsilon_3 &\equiv n_{\rm qs}(W_3)/n_{\rm qs}(W_{\rm c}) = n_{\rm s}(W_3)/n_{\rm s}(W_{\rm c}),\end{aligned} \tag{18}$$

with different $\tau_{\rm L}$, Φ, and I values, and build a database for pulse measurement. Here, $n_{\rm s}(W)$ is directly smoothed from the calculated or measured $n(W)$ values, which are not divided by the factor ΔT^2. The values of (ε_1, ε_2, ε_3)=(53.153%, 46.891%, 57.530%) are tagged in Fig. 3. Table 1 shows the SI data corresponding to ε_1, ε_2, and ε_3 calculated with $\lambda_{\rm L} =$ 750 nm, $\tau_{\rm L} = 7$ fs, $\Phi = 0°$, $\omega_{\rm X} = 1$ keV, and different laser intensities I. These data indicate that $\varepsilon_{1,2,3}$ change slightly as I changes (Φ is close to 0 or π). For example, (ε_1, ε_2, ε_3) change from (57.979%, 55.424%, 70.564%) to (52.390%, 46.419%, 46.074%) as I changes from 10^{13} to 1.5×10^{15} W/cm^2 with $\tau_{\rm L} = 7$ fs and $\Phi = 0$. For simplicity, using the half-maximum peak positions (W_1', W_2', W_3') (i.e., $n_{\rm s}(W'_{1,2,3}) = 0.5n_{\rm s}(W_{\rm a,b,c})$, where $n_{\rm s}(W)$ is a measured PES (calculated here)) instead of (W_1, W_2, W_3), equation (16) gives the initial solutions ($\tau_{\rm L}$, Φ, I)$_1$=(7.153 fs, 1.679°, 4.984×10^{14} W/cm^2). With these firstly calculated solution data ($\tau_{\rm L}$, Φ, I)$_1$ and the X-ray energy $\omega_{\rm X}$, we can (i) theoretically calculate a new PES $n'(W)$ within the SFA and its smoothed one $n'_{\rm S}(W)$, and find out its classical predictions (ε_1, ε_2, ε_3)$_1$ or directly search for (ε_1, ε_2, ε_3)$_1$ from a database according to the first solutions (τ_L, Φ, I)$_1$, (ii) read out the spectral positions (W_1, W_2, W_3)$_1$ according to (ε_1, ε_2, ε_3)$_1$=(52.215%, 47.552%, 52.998%) from the measured $n_{\rm s}(W)$, and (iii) recalculate ($\tau_{\rm L}$, Φ, I) with (W_1, W_2, W_3)$_1$ by using Eqs. (2). The final solutions for ($\tau_{\rm L}$, Φ, I) are ($\tau_{\rm L}$, Φ, I)$_2$=(7.075 fs, −0.341°, 4.997×10^{14} W/cm^2), which are in good agreement with the input data of (7 fs, 0°, 5×10^{14} W/cm^2). These procedures can be used to build a pulse with $\tau_{\rm L}$ as short as an optical cycle (e.g., 2.5 fs) or less.

Table 1. SI data corresponding to ε_1, ε_2, and ε_3, calculated at $\lambda_{\rm L} = 750$ nm, $\tau_{\rm L} = 7$ fs, $\Phi = 0°$, $\omega_{\rm X} = 1$ keV, and different laser intensities I.

I/W·cm^{-2}	ε_1/%	ε_2/%	ε_3/%
10^{13}	57.979	55.424	70.564
5×10^{13}	56.387	53.463	59.028
10^{14}	54.609	51.013	65.463
4.984×10^{14}	52.215	47.552	52.998
5×10^{14}	53.153	46.891	57.530
10^{15}	52.983	46.019	53.606
1.5×10^{15}	52.390	46.419	46.074

3.4. CEP and intensity dependence of the XBP energetic properties

Figure 4(a) shows SI data for an XBP PES, $n(W)$, calculated with the laser wavelength $\lambda_{\rm L} = 750$ nm, $\tau_{\rm L} = 7$ fs, $I = 5\times10^{14}$ W/cm^2, $\Phi = 270°$, and $\omega_{\rm X} = 1$ keV. Comparing this figure with Fig. 2(c) ($\Phi = 0°$ PES), the $\Phi = 270°$ PES have different structures and cut-off energies. The solid and dotted lines in Fig. 4(b) present $n_{\rm qs}(W)$ and the semi-classical prediction $n_{\rm sc}(W)$ for $\Phi = 270°$, respectively. These figures reveal large differences between $n_{\rm qs}(W)$ (which is adjacently (8 eV) averaged from $n_{\rm q}(W) = n(W)/\Delta T^2$) and its semi-classical prediction $n_{\rm sc}(W)$. The peak positions ($W_{\rm a}$, $W_{\rm b}$, $W_{\rm c}$) are much lower than their semi-classically predicted values (W_1, W_2, W_3). Because the field envelopes $F(t)$ are the same for the $\Phi = 0°$ and $\Phi = 270°$ PES calculations, different PES patterns reflect the sensitive dependence of the XBP energetic properties on the CEP.

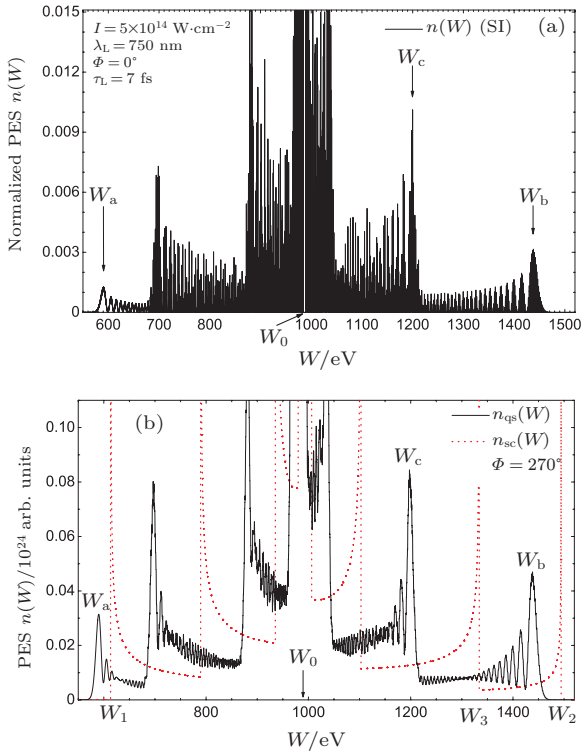


Fig. 4. (color online) PES energy properties. (a) Black line: SI data based on $n(W)$ (normalized). (b) Solid line: $n_{\rm qs}(W)$, which is smoothed from $n_{\rm q}(W) = n(W)/\Delta T^2$. Dotted line: the semi-classical prediction $n_{\rm sc}(W)$. $n(W)$ and $n_{\rm sc}(W)$ are calculated with $\lambda_{\rm L} = 750$ nm, $\tau_{\rm L} = 7$ fs, $I = 5\times10^{14}$ W/cm^2, $\omega_{\rm X} = 1$ keV, and $\Phi = 270°$.

There is another way to quickly determine Φ from the calculated line of $W_{\rm a}$ ($W_{\rm b}$) versus Φ according to the measured SI value of $W_{\rm a}$ ($W_{\rm b}$). For example, the open (filled) circles in Fig. 5(a) show SI $W_{\rm a}$ ($W_{\rm b}$) values calculated with $\lambda_{\rm L} = 750$ nm, $\tau_{\rm L} = 7$ fs, $I = 5\times10^{14}$ W/cm^2, and $\Phi = 0°$–360° (data in 0°–90° are shifted to 360°–450°). Similar to Fig. 5(a), the data shown in Fig. 5(b) are calculated with $I = 5\times10^{13}$ W/cm^2. According to these plots, (i) the values of $W_{\rm a}$ and $W_{\rm b}$ are sensitive to Φ, and (ii) the values of $W_{\rm a}$ ($W_{\rm b}$) and those corresponding to the semi-classical prediction W_1 (W_2) behave very differently as Φ changes. The $W_{\rm a}$ and $W_{\rm b}$ are near their semi-classically predicted values W_1 and W_2 only at $\Phi = 0°$ and 180°. The differences between the lines $W_{\rm a}$ ($W_{\rm b}$) versus Φ and W_1 (W_2) versus Φ indicate that quantum interference plays an important role in determining the XBP spectral structures and cut-off energies.

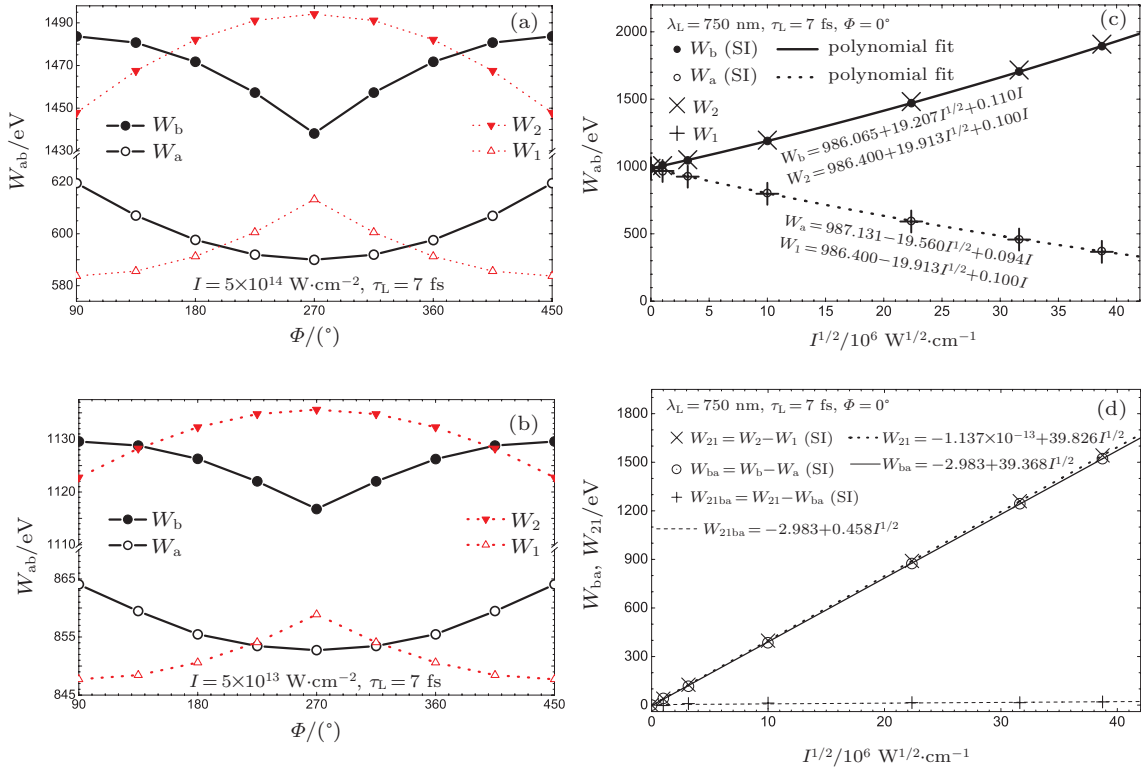


Fig. 5. (color online) PES cut-off energies W_a and W_b and their classically predicted values W_1 and W_2. (a) SI data calculated with $\tau = 7$ fs and $I = 5\times10^{14}$ W/cm^2. Open (filled) circles: data corresponding to W_a (W_b) versus Φ. Open (filled) triangles: data corresponding to W_1 (W_2) versus Φ. (b) Similar to (a), SI data calculated with $\tau_L = 7$ fs and $I = 5\times10^{13}$ W/cm^2. (c) Open (filled) circles: SI data corresponding to W_a (W_b) versus $I^{1/2}$. Dotted (solid) line is quadratically fitted from the data of W_a (W_b). '+' ('×') crosses: the semi-classically predicted values W_1 (W_2) corresponding to W_a (W_b). (d) The PES energy widths. '×' crosses (open circles): SI data corresponding to W_{21} (W_{ba}) versus $I^{1/2}$, where $W_{21}\equiv W_2 - W_1$ ($W_{ba}\equiv W_b - W_a$). Dotted (solid) line is linearly fitted from the data of W_{21} (W_{ba}). '+' crosses: SI data corresponding to W_{21ba} vs. $I^{1/2}$, where $W_{21ba}\equiv W_{21} - W_{ba}$. Dashed line is linearly fitted from the data of W_{21ba}.

With a known CEP Φ that has been measured and/or locked, the laser intensity I can be determined from the calculated slope of W_a (W_b) versus $I^{1/2}$ using the measured SI values of W_a (W_b). For example, the open (filled) circles in Fig. 5(c) show the SI W_a (W_b) values calculated with $\lambda_L = 750$ nm, $\tau_L = 7$ fs, $\Phi = 0°$, and $I = 1\times10^{12}$–1.5×10^{15} W/cm^2. The dotted and solid lines are quadratic curves fitted to W_a and W_b, respectively. From Eq. (9), the semi-classically predicted values W_1 and W_2 can be calculated with $\omega_L t + \Phi = -\pi/2$ and $\pi/2$ as follows:

$$W_1 = W_0 - \frac{2\sqrt{W_0}}{\omega_L}F\left(-\frac{\pi}{2\omega_L}\right)I^{1/2} + \frac{1}{\omega_L^2}F^2\left(-\frac{\pi}{2\omega_L}\right)I,$$
$$W_2 = W_0 + \frac{2\sqrt{W_0}}{\omega_L}F\left(\frac{\pi}{2\omega_L}\right)I^{1/2} + \frac{1}{\omega_L^2}F^2\left(\frac{\pi}{2\omega_L}\right)I. \quad (19)$$

For the current laser parameters ($\lambda_L = 750$ nm, $\tau_L = 7$ fs, $\Phi = 0°$), W_1 and W_2 have the following expressions:

$$W_1 = 986.400 - 19.913I^{1/2} + 0.100I,$$
$$W_2 = 986.400 + 19.913I^{1/2} + 0.100I, \quad (20)$$

where the units of I are 10^{12} W/cm^2. The '+' and '×' crosses in Fig. 5(c) show the values of W_1 and W_2, respectively. Quantitatively, the W_a values are up-shifted from W_1, while the W_b values are down-shifted from W_2 due to quantum interference. Table 2 shows the calculated SI data for (W_a, W_b) and the semi-classically predicted values (W_1, W_2).

Table 2. SI data corresponding to (W_a, W_b) and the semi-classically predicted values (W_1, W_2), calculated with $\lambda_L = 750$ nm, $\tau_L = 7$ fs, $\Phi = 0°$, $\omega_X = 1$ keV, and different laser intensities I.

I/W·cm^{-2}	W_1/eV	W_a/eV	W_b/eV	W_2/eV
10^{12}	966.587	965.229	1007.547	1006.414
10^{13}	924.434	928.814	1045.290	1050.376
10^{14}	797.319	802.716	1188.492	1195.581
4.984×10^{14}	591.440	597.800	1471.480	1481.480
5×10^{14}	591.280	597.600	1471.720	1482.120
10^{15}	457.192	459.581	1703.724	1716.607
1.5×10^{15}	365.919	371.590	1894.293	1908.380

From Eqs. (19), we obtain the semi-classically predicted value of the PES energy width as

$$W_{21}\equiv W_2 - W_1 = \frac{4\sqrt{W_0}}{\omega_L}F\left(\frac{\pi}{2\omega_L}\right)I^{1/2}. \quad (21)$$

For the current laser parameters,

$$W_{21} = 39.826I^{1/2}. \quad (22)$$

The '×' crosses in Fig. 5(d) show the SI W_{21} data. The dotted line is linearly fitted from W_{21} versus $I^{1/2}$. For comparison, the open circles in Fig. 5(d) show the data of the PES energy

width, $W_{ba} \equiv W_b - W_a$. The solid line is linearly fitted from W_{ba} versus $I^{1/2}$. The '+' crosses in Fig. 5(d) present the differences between W_{21} and W_{ba}, i.e., $W_{21ba} \equiv W_{21} - W_{ba}$, which quantitatively describe the effect of quantum interference on the spectrum. The dashed line is linearly fitted to W_{21ba} versus $I^{1/2}$. According to these plots and the linear fit expressions for W_{ba} versus $I^{1/2}$ (solid line) and W_{21ba} versus $I^{1/2}$ (dashed line), (i) W_{21}, W_{ba}, and their difference W_{21ba} depend linearly on $I^{1/2}$, and (ii) the relative difference between W_{ba} versus $I^{1/2}$ and W_{21} versus $I^{1/2}$ is $W_{21ba}/W_{ba} \equiv 0.458I^{1/2}/29.368I^{1/2} = 1.163\%$. Thus, the square root of the laser intensity ($I^{1/2}$), which is determined from W_{ba} versus $I^{1/2}$, instead of from W_{21} versus $I^{1/2}$, has a relative difference of -1.163% if the CEP Φ is locked to 0° or 180°, or $I^{1/2}$ can be exactly determined from W_{ba} versus $I^{1/2}$ with a relative correction of $+1.163\%$. More calculations with different CEP Φ values verified the above conclusion that $W_{ba} \propto I^{1/2}$ and validated the procedure of determining $I^{1/2}$ from the SI PES energy width W_{ba}.

4. Conclusion

A few-cycle intense laser pulse leaves a clear fingerprint of the field envelope $F(t)$ on an SI XBP PES as it passes though a gas. The laser pulse in the XBP simply acts as a nonlinear photoelectron energy modulator, and the ATI is only a background of the XBP. The field modulation and strong quantum interference collaboratively produce interesting PES structures and useful energetic properties. The field modulation determines the overall spectral distribution, while quantum interference determines the local structures and fluctuations. The SI PES energy width W_{ba} ($= W_b - W_a$) is linearly and sensitively dependent on the square root of the laser intensity I, namely, $W_{ba} \propto I^{1/2}$. The precise *in-situ* measurement of an intense laser pulse can be achieved using a simplified algorithm to reconstruct the pulse profile from a measured PES. Although the simulations are performed with $I < 10^{16}$ W/cm^2, the methods can work with I values up to 10^{18} W/cm^2 using higher-energy X-rays and highly charged inert gases, as long as the Lorentz force does not play a role in the motion of photoelectrons.

References

[1] Fuji T, Unterhuber A, Yakovlev V S, Tempea G, Stingl A, Krausz F and Drexler W 2003 *Appl. Phys. B* **77** 125
[2] Krauss G, Lohss S, Hanke T, Sell A, Eggert S, Huber R and Leitenstorfer A 2010 *Nat. Photon.* **4** 33
[3] Yanovsky V, Chvykov V, Kalinchenko G, Rousseau P, Planchon T, Matsuoka T, Maksimchuk A, Nees J, Cheriaux G, Mourou G and Krushelnick K 2008 *Opt. Eexpress* **16** 2109
[4] Wiehle R, Witzel B, Helm H and Cormier E 2003 *Phys. Rev. A* **67** 063405
[5] Spielmann C and Burnett N H 1997 *Science* **278** 661
[6] Schnuürer M, Spielmann C, Wobrauschek P, Streli C, Burnett N H, Kan C, Ferencz K, Koppitsch R, Cheng Z, Brabec T and Krausz F 1998 *Phys. Rev. Lett.* **80** 3236
[7] Kienberger R, Goulielmakis E, Uiberacker M, Baltuska A, Drescher M and Krausz F 2005 *J. Mod. Opt.* **52** 261
[8] Bula C, McDonald K T, Prebys E J, Bamber C, Boege S, Kotseroglou T, Melissinos A C, Meyerhofer D D, Ragg W, Burke D L, Field R C, Horton-Smith G, Odian A C, Spencer J E, Walz D, Berridge S C, Bugg W M, Shmakov K and Weidemann A W 1996 *Phys. Rev. Lett.* **76** 3116
[9] Mourou G and Tajima T 2011 *Science* **331** 41
[10] Florian A, Konstantinos M, Alfred L, Harald S, Burghard L, Gesine G and Florian T 2004 *Opt. Express* **12** 5872
[11] Ryu H Y, Moon H S and Suh H S 2007 *Opt. Express* **15** 11396
[12] Ryu H Y, Lee S H, Lee W K, Moon H S and Suh H S 2008 *Opt. Express* **16** 2867
[13] Diels J M, Fontaine J J, McMichael I C and Simoni F 1985 *Appl. Opt.* **24** 1270
[14] Pablo G and Rick T 2008 *JOSA B* **25** A25
[15] Lane R G and Tallon M 1992 *Appl. Opt.* **31** 6902
[16] Elster C and Weingartner I 1999 *Appl. Opt.* **38** 5024
[17] Chanteloup J C 2005 *Appl. Opt.* **44** 1559
[18] L'Huillier A, Lompre L A, Mainfray G and Manus C 1983 *J. Phys. B* **16** 1363
[19] Link A, Chowdhury E A, Morrison J T, Ovchinnikov V M, Offermann D, Woerkom L V, Freeman R R, Pasley J, Shipton E, Beg F, Rambo P, Schwarz J, Geissel M, Edens A and Porter J L 2006 *Rev. Sci. Instrum.* **77** 10E723
[20] Akahane Y, Ma J, Fukuda Y, Aoyoma M, Kiriyama H, Sheldakova J V, Kudryashov A V and Yamakawa K 2006 *Rev. Sci. Instrum.* **77** 023102
[21] Alnaser A S, Tong X M, Osipov T, Voss S, Maharjan C M, Shan B, Chang Z and Cocke C L 2004 *Phys. Rev. A* **70** 023413
[22] Smeenk C, Salvail J Z, Arissian L, Corkum P B, Hebeisen C T and Staudte A 2011 *Opt. Express* **19** 9336
[23] Lewenstein P, Balcou P, Ivanov M Y, L'Huillier A and Corkum P B 1994 *Phys. Rev. A* **49** 2117
[24] Chang Z, Rundquist A, Wang H, Murnane M M and Kapteyn H C 1997 *Phys. Rev. Lett.* **79** 2967
[25] Perry M D and Mourou G 1994 *Science* **264** 917
[26] Mashiko H, Suda A and Midorikawa K 2004 *Opt. Lett.* **29** 1927
[27] Tong X and Lin C 2005 *J. Phys. B: At. Mol. Opt. Phys.* **38** 2593
[28] Agostini P, Fabre F, Mainfray G, Petite G and Rahman N K 1979 *Phys. Rev. Lett.* **42** 1127
[29] Guo D S 2013 *Phys. Rev. Lett.* **110** 063002